On computational homogenization of microscale crack propagation

Citation for the original published paper (version of record):
Svenning, E., Fagerström, M., Larsson, F. (2016). On computational homogenization of microscale crack propagation. International Journal for Numerical Methods in Engineering, 108(1): 76-90. http://dx.doi.org/10.1002/nme.5220

INTERNATIONAL JOURNAL FOR NUMERICAL METHODS IN ENGINEERING
Int. J. Numer. Meth. Engng 2016; **108**:76–90
Published online 18 February 2016 in Wiley Online Library (wileyonlinelibrary.com). DOI: 10.1002/nme.5220

On computational homogenization of microscale crack propagation

Erik Svenning*,†, Martin Fagerström and Fredrik Larsson

Division of Material and Computational Mechanics, Department of Applied Mechanics, Chalmers University of Technology, Gothenburg, Sweden

SUMMARY

The effective response of microstructures undergoing crack propagation is studied by homogenizing the response of statistical volume elements (SVEs). Because conventional boundary conditions (Dirichlet, Neumann and strong periodic) all are inaccurate when cracks intersect the SVE boundary, we herein use first order homogenization to compare the performance of these boundary conditions during the initial stage of crack propagation in the microstructure, prior to macroscopic localization. Using weakly periodic boundary conditions that lead to a mixed formulation with displacements and boundary tractions as unknowns, we can adapt the traction approximation to the problem at hand to obtain better convergence with increasing SVE size. In particular, we show that a piecewise constant traction approximation, which has previously been shown to be efficient for stationary cracks, is more efficient than the conventional boundary conditions in terms of convergence also when crack propagation occurs on the microscale. The performance of the method is demonstrated by examples involving grain boundary crack propagation modelled by conventional cohesive interface elements as well as crack propagation modelled by means of the extended finite element method in combination with the concept of material forces. © 2016 The Authors. International Journal for Numerical Methods in Engineering Published by John Wiley & Sons Ltd.

Received 29 May 2015; Revised 13 January 2016; Accepted 13 January 2016

KEY WORDS: XFEM; multiscale modelling; microcracks; computational homogenization; weak periodicity; material forces

1. INTRODUCTION

The search for accurate and cost effective ways to model the response of microheterogeneous materials has attracted considerable interest for several years. The research efforts have lead to development of computational homogenization techniques [1, 2], where numerical simulations on a statistical volume element (SVE)[‡] have emerged as a standard tool. A critical aspect of such simulations, which is addressed in the present work, is the choice of suitable boundary conditions (BCs) on the SVE. We remark that the choice of BCs is particularly important when damage progression occurs in the microstructure, because the classical choices (Neumann, Dirichlet and (strong) periodic BCs [3, 4]) are inadequate in this case. On the one hand, Neumann BCs lead to spurious softening if damage evolves close to the SVE boundary, see [5] for an illustrative example. On the other hand, Dirichlet BCs suppress crack opening and damage progression at the SVE boundary, leading to overstiff predictions. Similarly, strong periodic BCs in standard form also suppress crack opening and localization unless the localization band is aligned with the periodicity directions, thereby leading to overstiff predictions in the general case. The overstiffening effect of artificial crack closure on the boundary can be severe for both Dirichlet and strong periodic BCs. In

*Correspondence to: Erik Svenning, Department of Applied Mechanics, Chalmers University of Technology, SE-41296 Gothenburg, Sweden.

†E-mail: erik.svenning@chalmers.se

‡We note that both *Representative Volume Element*, *Statistical Volume Element* and *Microstructural Volume Element* [5] are used in the literature to denote a sample of the microstructure. To stress the fact that a sample of finite size may not be truly representative, we prefer the notion *Statistical Volume Element*, cf. Ostoja-Starzewski [6].

fact, Talebi *et al*. [7] argue that strong periodic BCs should not be used at all when a crack intersects the SVE boundary. Hence, good strategies are needed to overcome the deficiencies of conventional BCs in the presence of damage progression.

Some strategies to alleviate the shortcomings discussed earlier are reported in the literature. For example, if a single dominating failure path can be identified, a possibility is to apply percolation-path-aligned BCs [5, 8] that are aligned with the localization direction. We remark, however, that the application of such BCs requires that there is a unique localization direction to be identified. In the present work, we instead aim to develop a method that is suitable even if a single dominating failure path cannot be identified. This is the case when several boundary-intersecting cracks are present in the microstructure, in particular, at the early stage of crack propagation.

In the following, we consider damage progression in the SVE *prior* to localization and restrict ourselves to first order homogenization. Hence, we do not consider the related and difficult issue of localization in the SVE, cf. Coenen *et al*. [5, 8] in the context of the percolation-path-aligned BCs mentioned previously, or the multiscale aggregating discontinuities method by Belytschko *et al*. [9]. Note, however, that an accurate representation of damage progression prior to localization is a prerequisite for accurate modelling of localization.

Starting from the developments for stationary cracks in [10], we herein adopt the concept of weakly periodic BCs [11]. Using a mixed variational format with displacements and boundary tractions as unknowns, we consider the problem of adapting the traction approximation to the problem at hand in order to gain improved convergence with increasing SVE size. Inspired by the success of a piecewise constant traction approximation for stationary cracks [10], we extend this formulation to the case when crack propagation occurs in the microstructure. It turns out that a traction approximation that is piecewise constant between crack-boundary intersections and SVE corners leads to superior convergence with increasing SVE size compared with conventional BCs.

Regarding the modelling of damage progression in the SVE, we note that models based on (local or nonlocal) continuum damage as well as discrete cracks are available. Restricting our attention to discrete cracks, we note that the kinematic description can be realized through element embedded discontinuities [12], cohesive interface elements (i.e. inter-element cracks) [13], a discontinuous Galerkin formulation [14] or the extended finite element method (XFEM) [15–17]. In the present work, we consider grain boundary crack propagation modelled with cohesive interface elements and arbitrary crack propagation modelled by means of XFEM. The kinematic crack representation needs to be combined with a model describing crack propagation. To this end, we will consider material forces (see e.g. [18–20]) in combination with XFEM and cohesive zone models in combination with cohesive interface elements.

The remainder of the paper is organized as follows: in Section 2, we state the variational format of the single scale (fully resolved) problem (i.e. prior to the introduction of computational homogenization). We state the expression for the homogenized stress in Section 3 and discuss the mixed variational format pertinent to the microscale problem, including models for crack propagation and suitable choices for the traction approximation, in Section 4. The numerical studies in Section 5 lead us to the conclusions presented in Section 6.

2. SINGLE SCALE PROBLEM

To establish the weak form of the (quasistatic) momentum balance and to introduce the necessary notation, we consider a two dimensional domain[§] Ω with external boundary Γ and internal boundaries Γ_{int}, the latter representing cracks in the material. The internal boundaries consist of two-sided surfaces with predefined normal $\boldsymbol{n}_{int}$ as shown in Figure 1. We remark that no particular simplicity requirements are imposed on the cracks; they may branch and intersect each other as well as the domain boundary. Because the internal boundary consists of two-sided surfaces, it has a positive

[§]In the present work, we restrict ourselves to two-dimensional problems to simplify the representation of the cracks and the traction mesh. Note, however, that weakly periodic boundary conditions [21] as well as XFEM [22] are applicable to three-dimensional problems.

DOI: 10.1002/nme

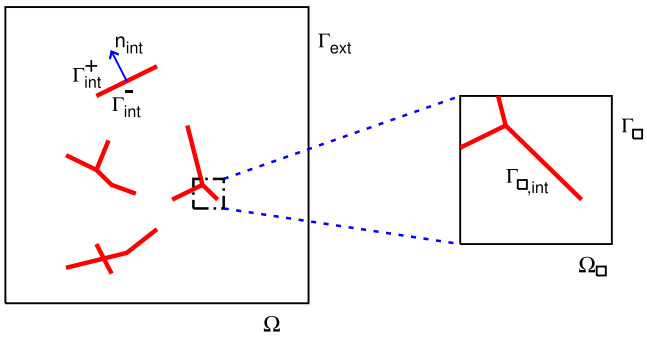

Figure 1. Domain Ω with external boundary Γ_{ext} and internal boundaries Γ_{int}. A statistical volume element with domain $\Omega_\square$ and boundary $\Gamma_\square$ is also shown.

side Γ^+_{int} and a negative side Γ^-_{int}. In the following, we let superscripts $^+$ and $^-$ denote quantities on Γ^+_{int} and Γ^-_{int}, respectively. For later use, we introduce the displacement jump over Γ_{int} as $[\![\boldsymbol{u}]\!] = \boldsymbol{u}^+ - \boldsymbol{u}^-$. We also introduce the small strain tensor $\boldsymbol{\epsilon} = [\boldsymbol{u} \otimes \boldsymbol{\nabla}]^{sym}$, where $\boldsymbol{\nabla}$ is the gradient operator.

Assuming quasistatic loading, small strains and neglecting the body force allow the equilibrium equations to be written in standard fashion as

$$\begin{aligned} -\boldsymbol{\sigma} \cdot \boldsymbol{\nabla} &= \boldsymbol{0} \text{ in } \Omega, \\ \boldsymbol{t}^+ + \boldsymbol{t}^- &= \boldsymbol{0} \text{ on } \Gamma_{int}, \\ \boldsymbol{t} \overset{\text{def}}{=} \boldsymbol{\sigma} \cdot \boldsymbol{n} &= \hat{\boldsymbol{t}} \text{ on } \Gamma_{ext,N}, \\ \boldsymbol{u} &= \hat{\boldsymbol{u}} \text{ on } \Gamma_{ext,D}, \end{aligned} \tag{1}$$

where $\boldsymbol{\sigma} = \boldsymbol{\sigma}(\boldsymbol{\epsilon})$ is the Cauchy stress, $\boldsymbol{n}$ is the outwards pointing normal vector, $\hat{\boldsymbol{t}}$ is a prescribed traction and $\hat{\boldsymbol{u}}$ is a prescribed displacement. On the internal boundaries, we have

$$\boldsymbol{t}^+ = -\boldsymbol{\sigma}|_{\Gamma^+_{int}} \cdot \boldsymbol{n}_{int} \quad \text{and} \quad \boldsymbol{t}^- = \boldsymbol{n}|_{\Gamma^-_{int}} \cdot \boldsymbol{n}_{int}, \tag{2}$$

where the traction $\boldsymbol{t} = \boldsymbol{t}^+ = -\boldsymbol{t}^-$ is given by a cohesive zone model in terms of the jump $[\![\boldsymbol{u}]\!]$. Here, $\boldsymbol{n}_{int}$ is defined as the outwards normal on Γ^-_{int}. In the case of traction free crack surfaces, we have $\boldsymbol{t} = \boldsymbol{0}$.

The weak solution to Equation (1) is obtained by finding $\boldsymbol{u} \in \mathbb{U}$ such that

$$\begin{aligned} \int_\Omega \boldsymbol{\sigma} : \delta\boldsymbol{\epsilon} \mathrm{d}\Omega - \int_{\Gamma^+_{int}} \boldsymbol{t} \cdot [\![\delta\boldsymbol{u}]\!] \mathrm{d}\Gamma &= \int_{\Gamma_{ext,N}} \hat{\boldsymbol{t}} \cdot \delta\boldsymbol{u} \, \mathrm{d}\Gamma \quad \forall \delta\boldsymbol{u} \in \mathbb{U}^0, \\ \mathbb{U} &= \left\{ \boldsymbol{v} : \boldsymbol{v} \in \left[\mathbb{H}^1(\Omega)\right]^d, \ \boldsymbol{v} = \hat{\boldsymbol{u}} \text{ on } \Gamma_{ext,D} \right\}, \\ \mathbb{U}^0 &= \left\{ \boldsymbol{v} : \boldsymbol{v} \in \left[\mathbb{H}^1(\Omega)\right]^d, \ \boldsymbol{v} = \boldsymbol{0} \text{ on } \Gamma_{ext,D} \right\}, \end{aligned} \tag{3}$$

where $\delta\boldsymbol{\epsilon} = [\delta\boldsymbol{u} \otimes \boldsymbol{\nabla}]^{sym}$, $\mathbb{H}^1(\Omega)$ denotes the (Sobolev) space of functions with square integrable gradients on Ω, and d denotes the dimension of the problem. We note that $\boldsymbol{u}$ and $\delta\boldsymbol{u}$ do not need to be continuous across Γ_{int}. In particular, discontinuities across Γ_{int} will be taken into account on the microscale as discussed later.

3. MACROSCALE PROBLEM

The variational format presented in Section 2 is valid for the single scale problem, where all microscale features are explicitly resolved. Aiming for multiscale modelling based on homogenizing the response of SVEs, we note that an expression for the effective macroscale stress needs to be

DOI: 10.1002/nme

derived. We neglect cracks on the macroscale and define $\bar{\Omega} \overset{\text{def}}{=} \Omega \cup \Gamma_{int}$, where $\bar{\Omega}$ is the homogeneous counterpart of Ω, not containing internal boundaries. We then introduce a running average according to

$$\int_{\Omega} y \mathrm{d}\Omega - \int_{\Gamma^+_{int}} z \mathrm{d}\Gamma \to \int_{\bar{\Omega}} \frac{1}{|\Omega_{\square}|} \left(\int_{\Omega_{\square}} y \mathrm{d}\Omega - \int_{\Gamma^+_{\square,int}} z \mathrm{d}\Gamma \right) \mathrm{d}\Omega, \tag{4}$$

where $\Omega_{\square}$ is an SVE, and $\Gamma^+_{\square,int} = \Gamma^+_{int} \cap \Omega_{\square}$ is the part of the internal boundary located inside $\Omega_{\square}$.

By applying the smoothing approximation given by Equation (4) to Equation (3), we obtain

$$\int_{\bar{\Omega}} \frac{1}{|\Omega_{\square}|} \left(\int_{\Omega_{\square}} \boldsymbol{\sigma} : [\delta \boldsymbol{u} \otimes \boldsymbol{\nabla}] \, \mathrm{d}\Omega - \int_{\Gamma^+_{\square,int}} \boldsymbol{t} \cdot [\![\delta \boldsymbol{u}]\!] \mathrm{d}\Gamma \right) \mathrm{d}\Omega = \int_{\Gamma_{ext,N}} \hat{\boldsymbol{t}} \cdot \delta \boldsymbol{u} \mathrm{d}\Gamma, \tag{5}$$

where we note that $\boldsymbol{\sigma} : \delta \boldsymbol{\epsilon} = \boldsymbol{\sigma} : [\boldsymbol{u} \otimes \boldsymbol{\nabla}]^{sym} = \boldsymbol{\sigma} : [\boldsymbol{u} \otimes \boldsymbol{\nabla}]$ due to the symmetry of $\boldsymbol{n}$.

To establish the macroscale problem, we define the homogenized variables

$$\bar{\boldsymbol{x}} = \frac{1}{|\Omega_{\square}|} \int_{\Omega_{\square}} \boldsymbol{x} \mathrm{d}\Omega, \qquad \bar{\boldsymbol{u}} \overset{\text{def}}{=} \frac{1}{|\Gamma_{\square}|} \int_{\Gamma_{\square}} \boldsymbol{u} \, \mathrm{d}\Gamma, \qquad \bar{\boldsymbol{u}} \otimes \boldsymbol{\nabla} \overset{\text{def}}{=} \frac{1}{|\Omega_{\square}|} \int_{\Gamma_{\square}} \boldsymbol{u} \otimes \boldsymbol{n} \, \mathrm{d}\Gamma, \tag{6}$$

where we note that $\bar{\boldsymbol{u}} \otimes \boldsymbol{\nabla}$ is not equal to the volume average of $\boldsymbol{u} \otimes \boldsymbol{\nabla}$ due to the presence of internal boundaries in the SVE. In standard fashion, the solution field in an SVE is split into a smooth macrofield part and a subscale fluctuation: $\boldsymbol{u} = \boldsymbol{u}^{\mathrm{M}} + \boldsymbol{u}^{\mathrm{s}}$. Using first order homogenization, it is assumed that the macrofield $\boldsymbol{u}^{\mathrm{M}}$ varies linearly in the SVE, so that it can be expanded in terms of the macroscopic displacement $\bar{\boldsymbol{u}}$ and the macroscopic displacement gradient $\bar{\boldsymbol{u}} \otimes \boldsymbol{\nabla}$ in the (macroscopic) point $\bar{\boldsymbol{x}}$ as $\boldsymbol{u}^{\mathrm{M}} = \bar{\boldsymbol{u}} + (\bar{\boldsymbol{u}} \otimes \boldsymbol{\nabla}) \cdot [\boldsymbol{x} - \bar{\boldsymbol{x}}]$ for any $\boldsymbol{x}$ in the SVE. Here, the homogenized field and its gradient thus define the macroscale field inside the SVE. We may now derive the macroscale problem by testing Equation (5) with test functions $\delta \boldsymbol{u}^{\mathrm{M}} = \delta \bar{\boldsymbol{u}} + (\delta \bar{\boldsymbol{u}} \otimes \boldsymbol{\nabla}) \cdot [\boldsymbol{x} - \bar{\boldsymbol{x}}]$ inside each SVE. The task is then to find $\bar{\boldsymbol{u}} \in \bar{\mathbb{U}}$ that solves

$$\begin{aligned} \int_{\bar{\Omega}} \bar{\boldsymbol{\sigma}} : [\delta \bar{\boldsymbol{u}} \otimes \boldsymbol{\nabla}] \, \mathrm{d}\Omega &= \int_{\Gamma_{ext,N}} \hat{\boldsymbol{t}} \cdot \delta \bar{\boldsymbol{u}} \, \mathrm{d}\Gamma \quad \forall \delta \bar{\boldsymbol{u}} \in \bar{\mathbb{U}}^0, \\ \bar{\mathbb{U}} &= \left\{ \boldsymbol{v} : \boldsymbol{v} \in \left[\mathbb{H}^1(\bar{\Omega}) \right]^d, \ \boldsymbol{v} = \hat{\boldsymbol{u}} \text{ on } \Gamma_{ext,D} \right\}, \\ \bar{\mathbb{U}}^0 &= \left\{ \boldsymbol{v} : \boldsymbol{v} \in \left[\mathbb{H}^1(\bar{\Omega}) \right]^d, \ \boldsymbol{v} = \boldsymbol{0} \text{ on } \Gamma_{ext,D} \right\}, \end{aligned} \tag{7}$$

where the effective macroscale stress is then given by

$$\bar{\boldsymbol{\sigma}} \overset{\text{def}}{=} \frac{1}{|\Omega_{\square}|} \int_{\Omega_{\square}} \boldsymbol{\sigma} \mathrm{d}\Omega. \tag{8}$$

In order to derive Equation (7), we have also assumed smooth boundary data in the sense that $\int_{\Gamma_{ext,N}} \hat{\boldsymbol{t}} \cdot \delta \boldsymbol{u} \mathrm{d}\Gamma = \int_{\Gamma_{ext,N}} \hat{\boldsymbol{t}} \cdot \delta \bar{\boldsymbol{u}} \mathrm{d}\Gamma$ and $\boldsymbol{u} = \bar{\boldsymbol{u}}$ on $\Gamma_{ext,D}$.

4. MICROSCALE PROBLEM

4.1. Mixed variational format

Section 3 specifies how to compute the effective stress based on the solution of the SVE problem. Here, we will specify the mixed variational format pertinent to the SVE problem. To facilitate imposition of weakly periodic BCs [10, 11], we divide the SVE boundary into an image

DOI: 10.1002/nme

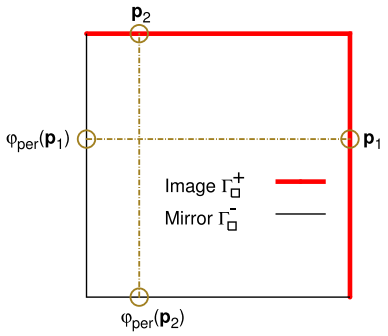

Figure 2. Statistical volume element with boundary divided into image and mirror parts.

part $\Gamma_\square^+$ and a mirror part $\Gamma_\square^-$ as shown in Figure 2. Furthermore, we introduce a mapping $\boldsymbol{\varphi}_{per} : \Gamma_\square^+ \rightarrow \Gamma_\square^-$ such that points on $\Gamma_\square^+$ and $\Gamma_\square^-$ are associated to each other according to $\boldsymbol{x}^- = \boldsymbol{\varphi}_{per}(\boldsymbol{x}^+)$. We also define the jump between a point $\boldsymbol{x}^+$ on $\Gamma_\square^+$ and the associated point $\boldsymbol{x}^- = \boldsymbol{\varphi}_{per}(\boldsymbol{x}^+)$ on $\Gamma_\square^-$ as[¶]

$$[\![\boldsymbol{u}]\!]_\square \overset{\text{def}}{=} \boldsymbol{u}_{\Gamma_\square^+} - \boldsymbol{u}_{\Gamma_\square^-}. \tag{9}$$

We may now state the requirements for periodicity as

$$[\![\boldsymbol{u}]\!]_\square = \bar{\boldsymbol{\epsilon}} \cdot [\![\boldsymbol{x} - \bar{\boldsymbol{x}}]\!]_\square \quad \text{on} \quad \Gamma_\square^+, \tag{10}$$

$$\boldsymbol{t}^+ + \boldsymbol{t}^- = \boldsymbol{0} \quad \text{on} \quad \Gamma_\square^+, \tag{11}$$

$$\frac{1}{|\Omega_\square|} \int_{\Gamma_\square} \boldsymbol{u} \, \mathrm{d}\Gamma = \boldsymbol{0}, \tag{12}$$

where $\bar{\boldsymbol{\epsilon}} \overset{\text{def}}{=} [\bar{\boldsymbol{u}} \otimes \boldsymbol{\nabla}]^{sym}$ is the effective strain. In the case of strong periodicity, Equations (10) and (11) are required to hold pointwise on $\Gamma_\square^+$. In the present work, we will only require weak fulfilment of Equation (10) (whereas Equation (11) will be fulfilled pointwise by construction). Thus, we introduce an independent discretization for the boundary traction. The SVE problem is then to find $\boldsymbol{u} \in \mathbb{U}_\square$ and $\boldsymbol{t}_\lambda \in \mathbb{T}_\square$ such that

$$\begin{aligned} a_\square(\boldsymbol{u}, \delta\boldsymbol{u}) - d_\square(\boldsymbol{t}_\lambda, \delta\boldsymbol{u}) &= 0 \quad \forall \delta\boldsymbol{u} \in \mathbb{U}_\square, \\ -d_\square(\delta\boldsymbol{t}_\lambda, \boldsymbol{u}) &= -d_\square(\delta\boldsymbol{t}_\lambda, \bar{\boldsymbol{\epsilon}} \cdot [\boldsymbol{x} - \bar{\boldsymbol{x}}]) \quad \forall \delta\boldsymbol{t}_\lambda \in \mathbb{T}_\square, \end{aligned} \tag{13}$$

$$\mathbb{U}_\square = \{\boldsymbol{v} : \boldsymbol{v} \in \left[\mathbb{H}^1(\Omega_\square)\right]^d, \int_{\Gamma_\square} \boldsymbol{v} \mathrm{d}\Gamma = \boldsymbol{0}\}, \tag{14}$$

$$\mathbb{T}_\square = \left\{\boldsymbol{v} : \boldsymbol{v} \in \left[\mathbb{L}_2\left(\Gamma_\square^+\right)\right]^d\right\}, \tag{15}$$

where we introduced the expressions

$$a_\square(\boldsymbol{u}, \delta\boldsymbol{u}) \overset{\text{def}}{=} \frac{1}{|\Omega_\square|} \left[\int_{\Omega_\square} \boldsymbol{\sigma} : \boldsymbol{\epsilon}[\delta\boldsymbol{u}] \, \mathrm{d}\Omega - \int_{\Gamma_{\square,int}^+} \boldsymbol{t} \cdot [\![\delta\boldsymbol{u}]\!] \mathrm{d}\Gamma \right], \tag{16}$$

[¶]Note that $[\![\boldsymbol{u}]\!]$ denotes the jump across an internal boundary Γ_{int}, whereas $[\![\boldsymbol{u}]\!]_\square$ denotes the jump over the external SVE boundary $\Gamma_\square$.

DOI: 10.1002/nme

$$d_{\square}(\boldsymbol{t}_{\lambda}, \delta\boldsymbol{u}) \overset{\text{def}}{=} \frac{1}{|\Omega_{\square}|} \int_{\Gamma_{\square}^{+}} \boldsymbol{t}_{\lambda} \cdot [\![\delta\boldsymbol{u}]\!]_{\square} \mathrm{d}\Gamma, \tag{17}$$

and $\mathbb{L}_2\left(\Gamma_{\square}^{+}\right)$ denotes the space of square integrable functions on $\Gamma_{\square}^{+}$.

Before proceeding, we remark that the Hill-Mandel macrohomogeneity condition is fulfilled for the weakly periodic BCs described previously [11]. To show that the Hill-Mandel condition indeed holds, we need to ensure that the volume average of the virtual work on the microscale equals the virtual work on the macroscale, that is,

$$a_{\square}(\boldsymbol{u}, \delta\boldsymbol{u}) = \bar{\boldsymbol{\sigma}} : \delta\bar{\boldsymbol{\epsilon}}. \tag{18}$$

To see this, insert the expansion $\delta\boldsymbol{u} = \delta\bar{\boldsymbol{u}} + (\delta\bar{\boldsymbol{u}} \otimes \boldsymbol{\nabla}) \cdot [\boldsymbol{x} - \bar{\boldsymbol{x}}] + \delta\boldsymbol{u}^{\mathrm{s}}$ in the expression for $a_{\square}(\boldsymbol{u}, \delta\boldsymbol{u})$ and note that $\delta\bar{\boldsymbol{u}}$ and $\delta\bar{\boldsymbol{u}} \otimes \boldsymbol{\nabla}$ are constant inside each SVE to obtain

$$a_{\square}(\boldsymbol{u}, \delta\boldsymbol{u}) = \bar{\boldsymbol{\sigma}} : \delta\bar{\boldsymbol{\epsilon}} + a_{\square}(\boldsymbol{u}, \delta\boldsymbol{u}^{\mathrm{s}}). \tag{19}$$

Hence, we need to show that $a_{\square}(\boldsymbol{u}, \delta\boldsymbol{u}^{\mathrm{s}}) = 0$. Using $\delta\boldsymbol{u}^{\mathrm{s}} = \delta\boldsymbol{u} - \delta\bar{\boldsymbol{u}} - (\delta\bar{\boldsymbol{u}} \otimes \boldsymbol{\nabla}) \cdot [\boldsymbol{x} - \bar{\boldsymbol{x}}]$ and Equation (13) gives the desired result.

4.2. Crack representation

To account for the presence of cracks in the SVE, we consider two strategies: XFEM and interface elements. For a discussion on interface elements, see e.g. [13]. As for XFEM modelling, we follow standard procedures (see e.g. the review in [17]) and use Heaviside enrichment in elements completely cut by a crack, whereas elements containing a crack tip are enriched with the asymptotic functions first proposed in [23]. In order to preserve the Kronecker-δ property of the discretization, we employ a shifted enrichment as first suggested in [24].

Regarding modelling of intersecting cracks, we remark that it is insufficient to add enrichments for each crack separately, without considering the other crack. To properly account for intersecting cracks, we use the same approach as Daux *et al*. [25], where *junction functions* are introduced at the intersection.

To model crack propagation, we consider (i) XFEM cracks in combination with the concept of material forces and (ii) cohesive zone elements. Next, we describe the material force crack propagation model used in the present work, followed by the cohesive zone model adopted.

4.3. Crack propagation based on material forces

The possibility to combine an XFEM representation of cracks with different models for crack propagation was the topic of the classical work in [15] and has attracted considerable research interest in recent years. Here, we consider crack propagation driven by material forces, see e.g. [26], the algorithmic treatment in [19] or the discussion on different propagation strategies in [20]. Using the domain integral method and assuming that the bulk material is elastic, the material force $\boldsymbol{F}_{mat}$ is given by

$$\boldsymbol{F}_{mat} = -\int_{\omega} \boldsymbol{M} \cdot [\phi \otimes \boldsymbol{\nabla}] \, \mathrm{d}\Omega, \tag{20}$$

where $\boldsymbol{M}$ is the Newton–Eshelby stress tensor, ϕ is a weight function and ω is a suitable region around the crack tip. In a small strain setting, the Newton–Eshelby stress is given by (see e.g. [27])

$$\boldsymbol{M} = \psi \boldsymbol{I} - \boldsymbol{H}^{T} \cdot \boldsymbol{\sigma}, \tag{21}$$

where ψ is the strain energy in the material and $\boldsymbol{H} = \boldsymbol{u} \otimes \boldsymbol{\nabla}$ is the displacement gradient.

DOI: 10.1002/nme

Crack propagation models based on material forces can be formulated in different ways, see [20] for a few examples. Letting Δa denote the motion of a propagating crack tip during a time step and aiming for a simple propagation model, we choose to compute the crack increment as

$$\Delta a = \beta H\left(|\boldsymbol{F}_{mat}| - F_{mat}^{crit}\right)\frac{\boldsymbol{F}_{mat}}{|\boldsymbol{F}_{mat}|}, \tag{22}$$

where β is a predefined increment length, F_{mat}^{crit} is a material parameter determining the onset of crack propagation and $H(\bullet)$ is the Heaviside function. In short, the choice in Equation (22) implies that cracks propagate in the direction of the material force if the magnitude of the material force exceeds a critical value. If the update specified by Equation (22) is performed explicitly, that is, if the crack is propagated at the end of each time step, this model is very similar to the model denoted *explicit proportional extension* in [20], the only difference lies in the choice of increment length. In the present work, we make a modification in order to reduce the time step dependency: if crack propagation occurs during a time step, we recompute the time step as many times as needed for the cracks to stop growing.

4.4. Cohesive zone model

When interface elements are used to study crack propagation, we consider a damage-plasticity type of cohesive zone model. Before proceeding, we would like to remark that the present work does not rely on the use of a particular cohesive zone model, any model that incorporates damage could be used in principle. Hence, we only give a brief overview of the model chosen. Following [28], we adopt a scalar damage model and express the traction as $\boldsymbol{t} = (1-\alpha)\,\tilde{\boldsymbol{t}}$,where $\alpha \in [0,1]$ represents the damage in the cohesive zone and $\tilde{\boldsymbol{t}}$ is the nominal traction vector related to the undamaged material. Adopting a plasticity model allows us to express the nominal traction vector as $\tilde{\boldsymbol{t}} = \boldsymbol{K}\cdot(\boldsymbol{d} - \boldsymbol{d}^{p})$, where $\boldsymbol{K}$ is the (elastic) stiffness of the cohesive zone, $\boldsymbol{d}$ is the total displacement jump and $\boldsymbol{d}^{p}$ is the plastic part of the displacement jump. To complete the description of the cohesive zone model, a flow rule and a damage evolution rule need to be specified. We define the yield function of the cohesive zone material as

$$F = \sigma_f\left(\frac{\tilde{t}_t}{\gamma\sigma_f}\right)^2 + \sigma_f\left(\frac{\langle\tilde{t}_n\rangle}{\sigma_f}\right)^2 - \sigma_f, \tag{23}$$

where σ_f and γ are material parameters. Furthermore, $\tilde{t}_t$ and $\tilde{t}_n$ denote the tangential and normal components of the nominal traction vector, respectively. We use an associative flow rule given by $\dot{\boldsymbol{d}}^{p} = \lambda\frac{\partial F}{\partial\tilde{\boldsymbol{t}}}$, where λ is the plastic multiplier. The damage evolution in the cohesive zone is given by $\dot{\alpha} = \lambda/S$, where S is a material parameter that is calibrated such that the mode I fracture energy g_I is correct, see [29] for details. For the simple version of the cohesive zone model considered here, the fracture energies in mode I and mode II are equal.

4.5. Traction approximation

Having established the variational format including models for crack propagation, it remains to specify suitable choices for $\mathbb{U}_{\square}^{h}$ and $\mathbb{T}_{\square}^{h}$. We construct $\mathbb{U}_{\square}^{h}$ using a conventional finite element mesh. For the construction of $\mathbb{T}_{\square}^{h}$, we first note that strong periodicity is fulfilled in the continuous setting, because the second identity in Equation (13) is fulfilled for all $\delta\boldsymbol{t}_\lambda \in \mathbb{T}_{\square}$ so that $\boldsymbol{u} = \bar{\boldsymbol{\epsilon}}\cdot[\![\boldsymbol{x} - \bar{\boldsymbol{x}}]\!]_{\square}$ holds pointwise on $\Gamma_{\square}^{+}$ in this case. If we instead consider the type of BC applied on the SVE as a modelling choice, we note that coarsening of $\mathbb{U}_{\square}$ and $\mathbb{T}_{\square}$ allows different modelling choices. In particular, Dirichlet and Neumann BCs are obtained by restricting the spaces $\mathbb{U}_{\square}$ and $\mathbb{T}_{\square}$, respectively. More precisely, Neumann BCs are obtained as the coarsest possible traction discretization, with piecewise constant traction on each face of the SVE. Furthermore, BCs with attractive convergence properties can be constructed by adapting the coarsening of $\mathbb{T}_{\square}$ to the problem at hand. Noting that the Hill-Mandel macrohomogeneity condition is fulfilled for arbitrary choices of $\mathbb{U}_{\square}^{h}$

DOI: 10.1002/nme

and $\mathbb{T}^h_\square$ [11], we follow [10] and construct $\mathbb{T}^h_\square$ by creating a traction mesh on the SVE boundary as shown in Figure 3. We consider traction approximations that are piecewise linear or piecewise constant on each traction element. More precisely, we create the traction mesh based on the locations of some or all of the (displacement) nodes on the SVE boundary and points where cracks or grain boundaries intersect the SVE boundary as indicated in Figure 3. This approach allows different traction approximations to be created, ranging from a fine traction mesh if all traction nodes are retained (yielding results close to strong periodic BCs), to the coarsest possible traction mesh with nodes only at the SVE corners (corresponding to Neumann BCs). Two different traction discretizations on this form will be studied in detail in the numerical examples:

(1) A piecewise linear traction discretization, with traction nodes at all crack-boundary intersections and displacement node locations on the boundary, as shown in Figure 4(a). This approximation is stable [11] and gives a solution close to strong periodic BCs. It will be denoted *dense* in the following.
(2) A piecewise constant traction discretization, with traction discontinuities only at SVE corners and where cracks or grain boundaries intersect the SVE boundary, as shown in Figure 4. This discretization is stable and has shown promising results for stationary cracks in previous investigations by the authors [10]. It will be denoted *piecewise const.* in the following.

4.6. *Updating the traction approximation upon crack propagation*

Because crack propagation is considered in the present work, we remark that the traction discretization must be updated during the simulation as new cracks intersect the SVE boundary. Neglecting the traction discretization update may lead to spurious softening if a piece of the structure becomes

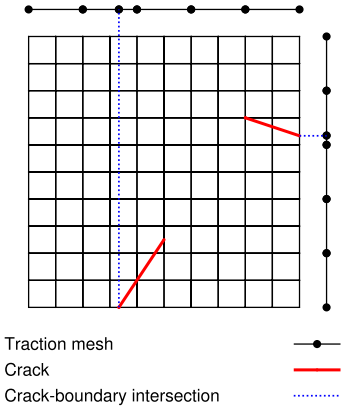

Figure 3. Example of a traction mesh created from (displacement) node locations on the boundary and positions of crack-boundary intersections.

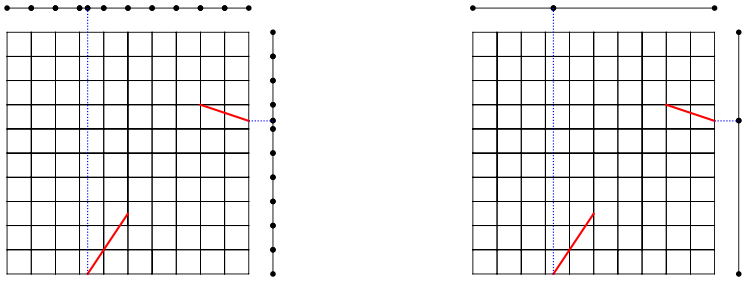

(a) Dense traction mesh with piecewise linear approximation, denoted *dense* in the following.

(b) Coarse traction mesh with piecewise constant approximation, denoted *piecewise const.* in the following.

Figure 4. Traction meshes considered in the numerical examples.

DOI: 10.1002/nme

completely cut loose by the propagating cracks. This observation is easily verified by starting with the coarsest possible traction discretization, corresponding to Neumann BCs. If the traction discretization is not updated when a propagating crack intersects the boundary, we have the case of Neumann BCs in combination with damage progression in the SVE, leading to a risk of spurious softening.

5. NUMERICAL EXAMPLES

In this section, we investigate the performance of different BCs when crack propagation occurs in the microstructure. The first example deals with a grain structure undergoing intergranular fracture modelled with cohesive zone elements, showing the overstiffening effect caused by Dirichlet BCs and strong periodic BCs, as well as the spurious softening caused by Neumann BCs. Next, we show an example of crack propagation modelled with XFEM and material forces, thus allowing us to study arbitrary crack propagation resulting in complex crack patterns. For the numerical implementation, we use the open source software package OOFEM [30, 31].

5.1. *Grain structure with intergranular fracture*

We consider a grain structure where the grains are elastic and cracks may propagate along the grain boundaries. For pre-processing, the open source software packages Neper [32, 33] and Phon [34] are used to generate grain structures and insert cohesive zone elements between the grains. We choose to model the grains as linear elastic with Poisson's ratio $\nu = 0.3$ and Young's modulus varying randomly within the range $E_0/100 \leqslant E \leqslant 100E_0$, where E_0 is a suitable reference modulus. The grain boundaries are modelled using the cohesive zone model described in Section 4.4, with initial stiffness $K = 1000E_0$, yield traction $\sigma_f = E_0/400$, fracture energy $g_I/E_0 = 1.0 \cdot 10^{-7}\ m$ and $\gamma = 0.5$. For the loading of the SVEs, we apply a uniaxial macroscopic strain of $\bar{\epsilon}_{xy} = 0.1\%$ in 100 load steps and monitor the effective stress component $\bar{\sigma}_{xy}$.

A typical FE mesh of a microstructure with grains is shown in Figure 5(a). The corresponding effective stress response is shown in Figure 5(b), where substantial nonlinearity due to the grain boundary damage evolution can be seen. (Recall that the bulk material is linear elastic in this example, hence all nonlinearity in Figure 5(b) stems from plasticity and damage in the grain boundaries.)

To investigate the average microstructure response, we consider different grain structure realizations like the one shown in Figure 5 and compute the average effective stress using both direct and inverse sampling. More precisely, direct sampling is obtained by computing the average as

$$\bar{\sigma}_{ij}^{D} = \frac{1}{N}\sum_{k=1}^{N} \bar{\sigma}_{ij,k}, \tag{24}$$

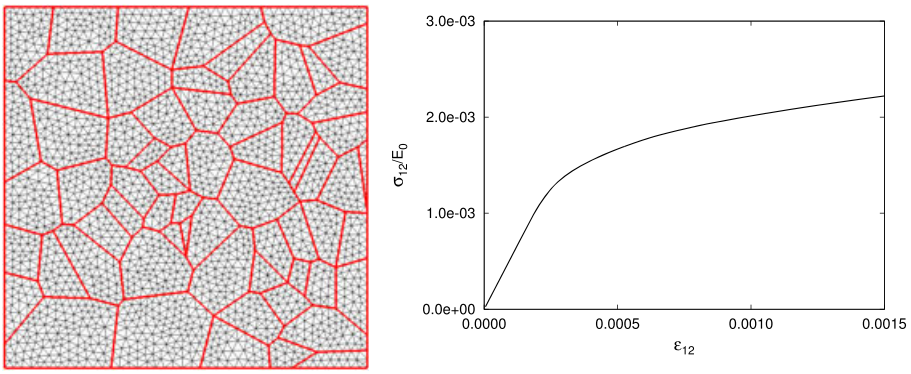

(a) Grain structure. (b) Effective response.

Figure 5. Example of a grain structure and the corresponding effective response.

DOI: 10.1002/nme

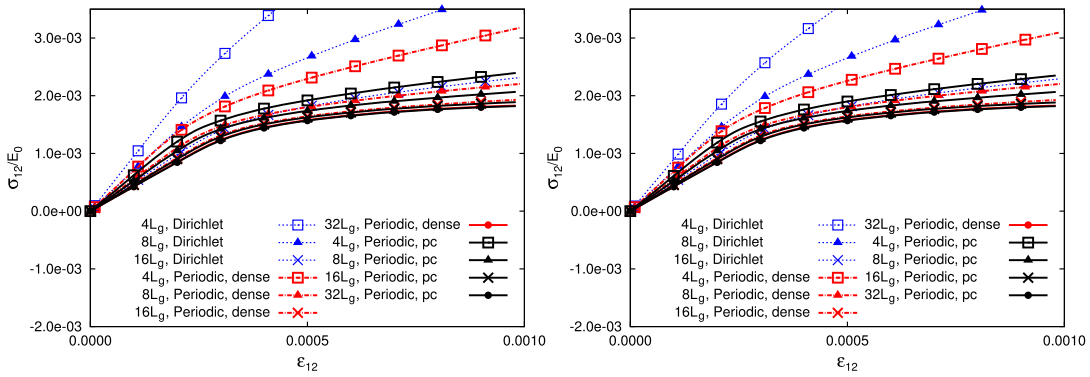

(a) Direct sampling. (b) Inverse sampling.

Figure 6. Average effective response of grain structures computed with weakly periodic boundary conditions and Dirichlet boundary conditions for different statistical volume element sizes.

where $\bar{\sigma}_{ij,k}$ is the ij-component of the $k:th$ realization. Inverse sampling is given by

$$\bar{\sigma}^I_{ij} = \left(\frac{1}{N} \sum_{k=1}^{N} \bar{\sigma}^{-1}_{ij,k} \right)^{-1}. \tag{25}$$

The motivation for studying both direct and inverse sampling is the following: direct sampling is completely analogous to (upper bound) Voigt sampling for given strain. Inverse sampling, on the other hand, 'mimics' the (lower bound) Reuss sampling strategy, which formally should be computed for given stress. Hence, the inverse sampling strategy can be expected to be closer to a lower bound estimate. For more details on Voigt and Reuss sampling, cf. [35].

The number of realizations for each SVE size is chosen such that the 95% confidence interval for the area under the effective stress–strain curve is within ±5% of the mean value. We compute the effective response for different SVE sizes, ranging from $L_\square = 4L_g$ to $L_\square = 32L_g$, where L_g is the average grain size and $L_\square$ is the side length of the SVE. From the results shown in Figure 6, we note that Dirichlet BCs are severely overstiff: the curves predicted with $L_\square = 4L_g$ and $L_\square = 8L_g$ are far above the corresponding curves computed with weakly periodic BCs. Using Dirichlet BCs, $L_\square$ needs to be as large as $16L_g$ to obtain results that are similar to the response obtained with weakly periodic BCs. Weakly periodic BCs perform much better: using $L_\square = 4L_g$ and a piecewise constant traction approximation gives results similar to using $L_\square = 16L_g$ in combination with Dirichlet BCs. We also note that weakly periodic BCs with a coarse, piecewise constant traction approximation performs better than weakly periodic BCs with dense traction approximation (corresponding to strong periodic BCs), in particular for the smaller SVE sizes ($L_\square = 4L_g$ and $L_\square = 8L_g$).

We conclude this example by noting that Neumann BCs (as expected) lead to spurious softening as shown in Figure 7. The severity of the spurious softening increases with increasing SVE size. Hence, weakly periodic BCs are more effective than Neumann, Dirichlet and strong periodic BCs when crack propagation occurs in the microstructure.

5.2. *Propagating XFEM cracks*

In the second example, we consider crack propagation in a linear elastic bulk material using XFEM and material forces. The purpose of the example is to investigate the performance of different BCs in situations where the final crack pattern, including the points where growing cracks will intersect the SVE boundary, cannot be determined a-priori. To this end, we consider randomly distributed cracks that are initially straight with an initial length L_c. A set of SVEs are generated by first creating a large microstructure sample and then cutting out SVEs of different sizes from the sample as shown in Figure 8. As can be seen, no extra regularity requirements are imposed on the crack pattern:

DOI: 10.1002/nme

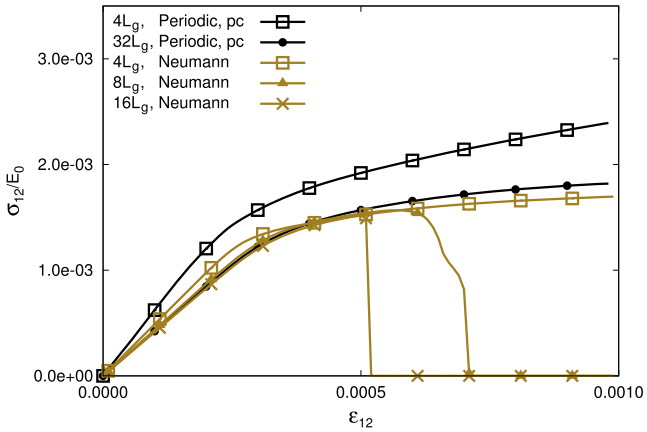

Figure 7. Average effective response of grain structures computed with Neumann boundary conditions and inverse sampling for different tatistical volume element sizes.

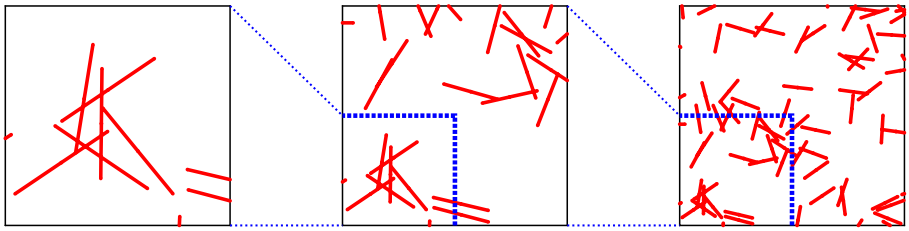

Figure 8. Statistical volume elements of different sizes for the random microstructure considered in Example 5.2.

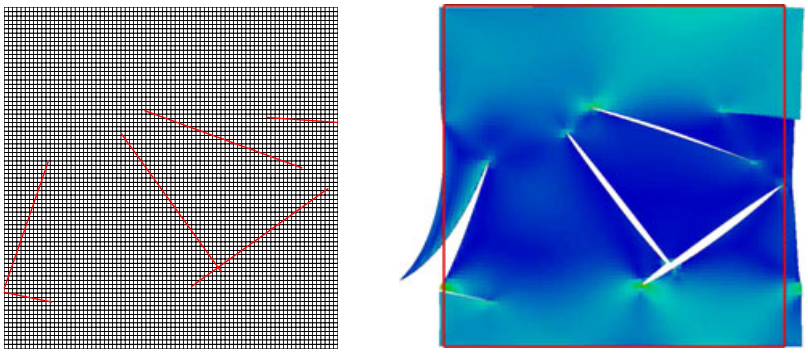

(a) Mesh used for the smallest SVE. (b) Deformed structure (with magnified deformation).

Figure 9. One of the statistical volume elements used in Example 5.2.

the orientations and positions of the cracks are completely random. Note that even though the cracks are (for simplicity of statistical sample generation) initially straight, they may propagate in arbitrary directions and will therefore not remain straight.

For the material parameters, we choose Young's modulus $E = E_0$ and Poisson's ratio $\nu = 0.3$. Furthermore, cracks propagate according to Equation (22) when the magnitude of the material force exceeds $F_{mat}^{crit}/E_0 = 1.0 \cdot 10^{-7}\ m^2$, and we set the increment length to $\beta = 0.05L_c$. A uniform mesh size of $h = 0.025L_c$ is used for all SVE sizes. This is a relatively fine mesh resolution, as shown in Figure 9(a), with 6400 elements for the smallest SVE with a side length of $L_\square = 2L_c$, and $4 \cdot 10^5$ elements for the largest SVE with side length $L_\square = 16L_c$. To improve the accuracy of the material force computation, we use branch enrichment in elements containing a crack tip as

DOI: 10.1002/nme

described previously. We remark that a much finer mesh would be required if only step enrichment were used.

As for the loading of the SVEs, we choose to apply a uniaxial macroscopic strain of $\bar{\epsilon}_{xx} = 0.25\%$ in 25 load steps and monitor the effective stress component $\bar{\sigma}_{xx}$. An example of a deformed SVE is shown in Figure 9(b).

Before presenting the main results of this section, we make a few remarks on the qualitative behaviour of the model. Because we consider growth of traction free cracks in an elastic material, the SVE will typically respond elastically for some load steps, until the crack driving force reaches the critical value. When the critical value is reached, one or several cracks start to propagate. The cracks will continue to grow until they reach a stable configuration or cross the SVE boundary. This results in a sudden drop in the effective stress when a crack propagates. The expected response of a single SVE is therefore an elastic response interrupted by sudden drops due to crack propagation. An example showing this type of response can be seen in Figure 10, which was computed using the SVE shown to the left in Figure 8. The crack pattern at different stages of the simulation is shown in Figure 11, where we note that the two large drops in the effective stress (seen in Figure 10) correspond to growth of a crack to the SVE boundary. When several SVE realizations are considered, averaging over many SVEs will produce a smoother response than that shown in Figure 10. For the same reason, we expect a smoother response if a single sufficiently large SVE is considered.

After these introductory remarks, we are now ready to proceed and study statistical properties of the microstructure. For this example, we will not consider Neumann BCs, because they predict zero effective stress as soon as a piece of the SVE is completely cut loose by cracks. Because this will always happen for a sufficiently large SVE, Neumann BCs converge to the (useless) lower bound of

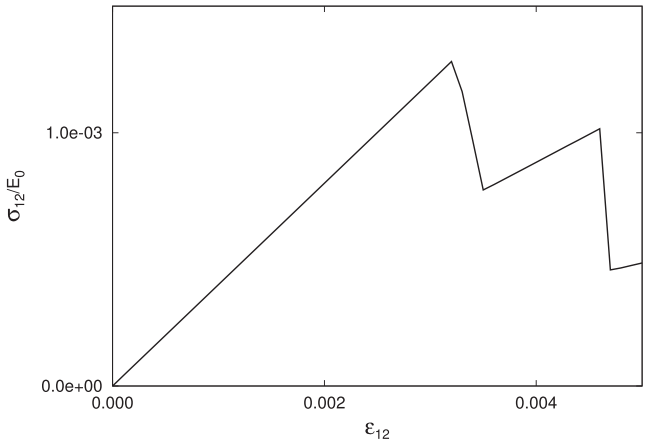

Figure 10. Response of a single statistical volume element. Crack propagation causes sudden drops in the otherwise elastic response.

(a) $\bar{\epsilon}_{xx} = 0\%$ (b) $\bar{\epsilon}_{xx} = 0.35\%$ (c) $\bar{\epsilon}_{xx} = 0.50\%$

Figure 11. Crack pattern at different stages of the simulation.

DOI: 10.1002/nme

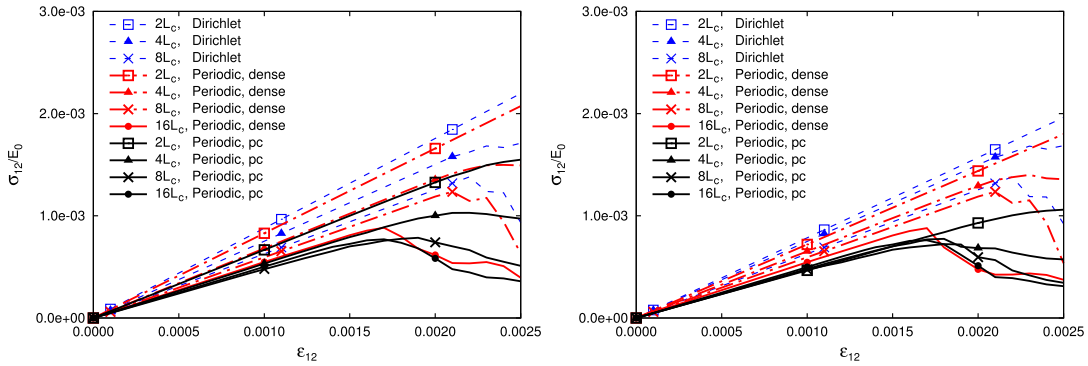

(a) Direct sampling. (b) Inverse sampling.

Figure 12. Average response of a microstructure with propagating cracks, computed with different boundary conditions and statistical volume element sizes.

zero stress for this example. In fact, Neumann BCs will predict zero effective stress for a random crack pattern even for stationary cracks (i.e. even if crack propagation is not considered), cf. [10].

As output from the simulations, we monitor the effective stress averaged over several SVEs, using both direct and inverse averaging. The number of realizations for each SVE size is chosen such that the 95% confidence interval for the area under the effective stress–strain curve is within $\pm 10\%$ of the mean value. The average effective stress, computed with different BCs and SVE sizes, is shown in Figure 12. We first note that the curves are not perfectly smooth. Because a typical SVE will respond as shown in Figure 10, a very large number of SVEs would be necessary to obtain perfectly smooth curves.

Comparing the results in Figure 12 for different BCs, we note that Dirichlet BCs give the stiffest response, as expected. Weakly periodic BCs with dense traction discretization (roughly corresponding to strong periodic BCs) perform slightly better, but the response is notably overstiff. Weakly periodic BCs with piecewise constant traction converge faster than both Dirichlet BCs and weakly periodic BCs with dense traction discretization. For example, using Direct sampling, the response predicted with $L_\square = 4L_c$ and piecewise constant traction approximation is closer to the converged solution than the response predicted with $L_\square = 8L_c$ and dense traction approximation. Using inverse sampling, a piecewise constant traction approximation convergences faster with increasing SVE size compared with using direct sampling. Hence, the results suggest that the SVE only needs to be less than half as large to obtain accurate results if a piecewise constant traction approximation is used, compared with using a dense traction approximation.

6. SUMMARY AND CONCLUSIONS

Computational homogenization of microstructures undergoing crack propagation is studied by homogenizing the response of SVEs. In particular, we are interested in finding suitable BCs on the SVE for the early stage of crack propagation in the microstructure (prior to macroscopic localization). We remark that the choice of BCs on the SVE is critical in this case, because conventional BCs (Dirichlet, Neumann and strong periodic) are inaccurate if cracks intersect the SVE boundary. As a remedy, we employ the concept of weakly periodic BCs [10, 11], leading to a mixed variational format with displacements and boundary tractions as unknowns. Following the developments for stationary cracks in [10], we employ a piecewise constant traction approximation that is dynamically updated as cracks propagate in the SVE. To be specific, the traction approximation is piecewise constant between crack-boundary intersections and SVE corners, thereby representing the smallest possible refinement of Neumann BCs.

The performance of the proposed method is demonstrated by numerical examples including conventional cohesive zone elements as well as crack propagation modelled by XFEM in combination

DOI: 10.1002/nme

with the material force concept. The results show that weakly periodic BCs with piecewise constant traction approximation yield superior convergence with increasing SVE size compared with Dirichlet, Neumann and strong periodic BCs. The results thereby indicate that a more efficient homogenization procedure can be obtained if the proposed BCs are utilized because a smaller SVE can be used for the same level of accuracy.

As for future developments, we believe that the challenging transition from damage to localization can be addressed within the framework employed here. In particular, we believe that the possibility to adapt the BCs to the evolving crack pattern by adapting the traction discretization, without having to identify a single dominating crack path, will be advantageous. Furthermore, the proposed framework does not require a periodic mesh. This is a clear advantage when crack propagation in the microstructure is considered.

ACKNOWLEDGEMENTS

The project is financially supported by the Swedish Research Council (www.vr.se) under contract 2012-3006. The simulations were performed on resources at Chalmers Centre for Computational Science and Engineering (C3SE) provided by the Swedish National Infrastructure for Computing (SNIC).

REFERENCES

1. Geers MGD, Kouznetsova VG, Brekelmans WAM. Multi-scale computational homogenization: trends and challenges. *Journal of Computational and Applied Mathematics* 2010; **234**(7):2175–2182.
2. Zohdi TI, Wriggers P. A model for simulating the deterioration of structural-scale material responses of microheterogeneous solids. *Computer Methods in Applied Mechanics and Engineering* 2001; **190**(22–23):2803–2823.
3. Fish J, Shek K, Pandheeradi M, Shephard MS. Computational plasticity for composite structures based on mathematical homogenization: theory and practice. *Computer Methods in Applied Mechanics and Engineering* 1997; **148**(1-2):53–73.
4. Miehe C, Koch A. Computational micro-to-macro transitions of discretized microstructures undergoing small strains. *Archive of Applied Mechanics (Ingenieur Archiv)* 2002; **72**(4–5):300–317.
5. Coenen EWC, Kouznetsova VG, Geers MGD. Novel boundary conditions for strain localization analyses in microstructural volume elements. *International Journal for Numerical Methods in Engineering* 2012; **90**(1):1–21.
6. Ostoja-Starzewski M. Material spatial randomness: from statistical to representative volume element. *Probabilistic Engineering Mechanics* 2006; **21**(2):112–132.
7. Talebi H, Silani M, Bordas SPA, Kerfriden P, Rabczuk T. A computational library for multiscale modeling of material failure. *Computational Mechanics* 2013; **53**(5):1047–1071.
8. Coenen EWC, Kouznetsova VG, Bosco E, Geers MGD. A multi-scale approach to bridge microscale damage and macroscale failure: a nested computational homogenization-localization framework. *International Journal of Fracture* 2012; **178**(1–2):157–178.
9. Belytschko T, Loehnert S, Song JH. Multiscale aggregating discontinuities: a method for circumventing loss of material stability. *International Journal for Numerical Methods in Engineering* 2008; **73**(6):869–894.
10. Svenning E, Fagerström M, Larsson F. Computational homogenization of microfractured continua using weakly periodic boundary conditions. *Computer Methods in Applied Mechanics and Engineering* 2016; **299**:1–21.
11. Larsson F, Runesson K, Saroukhani S, Vafadari R. Computational homogenization based on a weak format of micro-periodicity for RVE-problems. *Computer Methods in Applied Mechanics and Engineering* 2011; **200**(1–4):11–26.
12. Simo JC, Oliver J, Armero F. An analysis of strong discontinuities induced by strain-softening in rate-independent inelastic solids. *Computational Mechanics* 1993; **12**(5):277–296.
13. Ortiz M, Pandolfi A. Finite-deformation irreversible cohesive elements for three-dimensional crack-propagation analysis. *International Journal for Numerical Methods in Engineering* 1999; **44**(9):1267–1282.
14. Hansbo A, Hansbo P. A finite element method for the simulation of strong and weak discontinuities in solid mechanics. *Computer Methods in Applied Mechanics and Engineering* 2004; **193**(33–35):3523–3540.
15. Belytschko T, Black T. Elastic crack growth in finite elements with minimal remeshing. *International Journal for Numerical Methods in Engineering* 1999; **45**(5):601–620.
16. Babuska I, Caloz G, Osborn JE. Special finite element methods for a class of second order elliptic problems with rough coefficients. *SIAM Journal on Numerical Analysis* 1994; **31**(4):945–981.
17. Fries TP, Belytschko T. The extended/generalized finite element method: an overview of the method and its applications. *International Journal for Numerical Methods in Engineering* 2010; **84**(3):253–304.
18. Gurtin ME. The nature of configurational forces. *Archive for Rational Mechanics and Analysis* 1995; **131**(1):67–100.
19. Steinmann P, Ackermann D, Barth FJ. Application of material forces to hyperelastostatic fracture mechanics. II. Computational setting. *International Journal of Solids and Structures* 2001; **38**(32–33):5509–5526.
20. Brouzoulis Jim, Larsson Fredrik, Runesson Kenneth. Strategies for planar crack propagation based on the concept of material forces. *Computational Mechanics* 2010; **47**(3):295–304.

21. Öhman M, Runesson K, Larsson F. On the variationally consistent computational homogenization of elasticity in the incompressible limit. *Advanced Modeling and Simulation in Engineering Sciences* 2015; **2**(1):1–29.
22. Areias PMA, Belytschko T. Analysis of three-dimensional crack initiation and propagation using the extended finite element method. *International Journal for Numerical Methods in Engineering* 2005; **63**:760–788.
23. Moës N, Dolbow J, Belytschko T. A finite element method for crack growth without remeshing. *International Journal for Numerical Methods in Engineering* 1999; **46**(1):131–150.
24. Belytschko T, Moës N, Usui S, Parimi C. Arbitrary discontinuities in finite elements. *International Journal for Numerical Methods in Engineering* 2001; **50**(4):993–1013.
25. Daux C, Moës N, Dolbow J, Sukumar N, Belytschko T. Arbitrary branched and intersecting cracks with the extended finite element method. *International Journal for Numerical Methods in Engineering* 2000; **48**(12):1741–1760.
26. Maugin GA. Material forces: concepts and applications. *Applied Mechanics Reviews* 1995; **48**(5):213–245.
27. Heintz P, Larsson F, Hansbo P, Runesson K. Adaptive strategies and error control for computing material forces in fracture mechanics. *International Journal for Numerical Methods in Engineering* 2004; **60**(7):1287–1299.
28. Fagerström M, Larsson R. Theory and numerics for finite deformation fracture modelling using strong discontinuities. *International Journal for Numerical Methods in Engineering* 2006; **66**(6):911–948.
29. Larsson R, Fagerström M. A framework for fracture modelling based on the material forces concept with XFEM kinematics. *International Journal for Numerical Methods in Engineering* 2005; **62**(13):1763–1788.
30. Patzák B, Bittnar Z. Design of object oriented finite element code. *Advances in Engineering Software* 2001; **32**(10-11):759–767.
31. Patzák B. *OOFEM project home page:* www.oofem.org, 2000. [accessed on 29 May 2015].
32. Quey R. *Neper project home page:* http://neper.sourceforge.net. [accessed on 29 May 2015].
33. Quey R, Dawson PR, Barbe F. Large-scale 3D random polycrystals for the finite element method: generation, meshing and remeshing. *Computer Methods in Applied Mechanics and Engineering* 2011; **200**(17–20):1729–1745.
34. Carlsson K. *Phon project home page:* https://github.com/KristofferC/Phon.git. [accessed on 29 May 2015].
35. Saroukhani S, Vafadari R, Andersson R, Larsson F, Runesson K. On statistical strain and stress energy bounds from homogenization and virtual testing. *European Journal of Mechanics – A/Solids* 2015; **51**:77–95.

DOI: 10.1002/nme